ACS OMEGA

Open Access

http://pubs.acs.org/journal/acsodf

Article

Influence of Host Lattice Ions on the Dynamics of Transient Multiband Upconversion in Yb−Er Codoped $NaLnF_4$ and $LiLnF_4$ Microcrystals (Ln: Y, Lu, Gd)

Mingchen Li, Maohui Yuan, Wenda Cui, Hanchang Huang, Chuan Guo,* and Kai Han*

Cite This: *ACS Omega* 2024, 9, 39893−39903

Read Online

ACCESS | Metrics & More | Article Recommendations | Supporting Information

ABSTRACT: Inorganic host matrices provide a tunable luminescence environment for lanthanide ions, allowing for the modulation of upconversion luminescence (UCL) properties. $AREF_4$ (A = alkali metal, RE = rare earth) have a low phonon energy and a high optical damage threshold, making them widely used as the host matrix for UCL materials. However, the impact mechanism of alkali metal ions and lanthanide lattice ions on transient UCL dynamics in $AREF_4$ remains unclear. This study utilized a high-power nanosecond-pulsed laser at 976 nm to excite Yb−Er codoped $NaLnF_4$ and $LiLnF_4$ (Ln: Y, Lu, and Gd) microcrystals (MCs). All samples exhibit multiband emission, and the transient UC dynamics are discussed in detail. Compared with $LiLnF_4$, $NaLnF_4$ has higher UC efficiency and red to green (R/G) ratio. Lanthanide ions (Y, Lu, and Gd) affect the energy transfer (ET) distance in Yb−Er codoped systems, thereby altering UC efficiency and the R/G ratio. The energy level coupling between Gd^{3+} and Er^{3+} prolongs the duration of the UC emission. Specifically, the red emission lifetime of $NaGdF_4$ is five times longer than that of $NaYF_4$. Our research contributes to exploring excellent alternative host matrices for $NaYF_4$ in the fields of rapid-response optoelectronic devices, micro−nano lasers, and stimulated emission depletion (STED) microscopy.

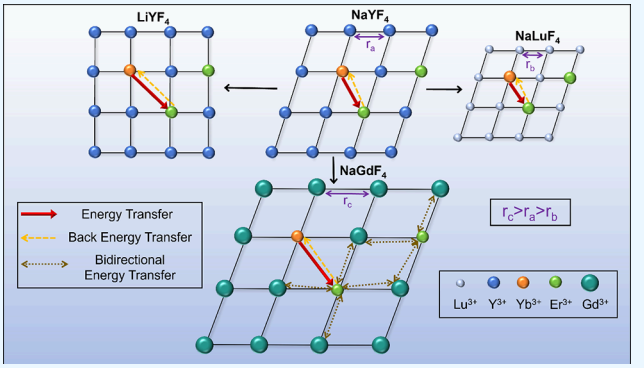

1. INTRODUCTION

In recent few years, lanthanide-doped upconverted inorganic host matrix materials, which have the ability to effectively convert two or more low-energy photons into one high-energy photon, have drawn widespread attention on their potential utilization in laser devices,[1−5] photovoltaic cells,[6−13] sensors,[14−23] biologies,[24−30] and therapeutics.[31−40] The upconversion (UC) process mainly relies on the ladder-like energy levels of doped rare earth ions. However, the crystal structure and optical properties of host matrices also play an important role in improving the UC efficiency: the excitation energy may be absorbed by the matrix vibration; the different lattice structures of the matrix can also lead to changes in the crystal field around the activator, thereby causing changes in the UC properties. An ideal matrix should possess the following characteristics: excellent transparency within a specific wavelength range, minimal phonon energy, and high optical damage threshold. Furthermore, to attain a high doping concentration, the matrix and doped ions must exhibit good lattice matching. Among diverse host matrices, lanthanide-doped fluoride materials ($AREF_4$, A = alkali metal, RE = rare earth) such as $NaYF_4$ possess not only magnificent optical properties but also glorious radiative efficiency with a phonon energy as low as 350 cm^{-1} and a quantum yield of up to 10%. However, host lattice manipulation, as a commonly used method for tuning UC luminescence (UCL) properties, has opened up a pathway to find excellent alternative materials for $NaYF_4$. For instance, Li^+ (0.073−0.106 nm) has a smaller radius than Na^+ (0.113−0.153 nm) and is widely used for doping to change the crystal field symmetry. Completely replacing Na^+ with Li^+ can minimize the size of the matrix materials and control the luminescence intensity, making $LiYF_4$ a good alternative host to $NaYF_4$. Several researchers have performed comparative studies on two different types of inorganic matrix materials. For instance, Wei et al. synthesized Yb−Er codoped $NaYF_4$ and $LiYF_4$ and conducted a comparative analysis of their morphology, UCL intensity, and red/green (R/G) ratio;[41] Wang et al. studied the effect of Li^+ doping concentration on the morphology, crystal structure, and UCL of $NaYF_4$:Yb/Er nanocrystals;[42] and Tsang et al. doped Pr^{3+} and Yb^{3+} into $NaYF_4$ and $LiYF_4$, achieving the combination of UC and

Received: June 11, 2024
Revised: August 21, 2024
Accepted: August 27, 2024
Published: September 10, 2024

downconversion (DC) luminescent properties, which can be used for biomedical applications.[43]

In addition, trivalent lanthanide ions also affect the crystal field characteristics, thereby changing the UCL of the host matrix. Except for Y^{3+}, common lanthanide host lattice ions also include Lu^{3+} and Gd^{3+}. Researchers have studied the inorganic host matrix of these ions. He et al. studied the UC and DC luminescence of β-NaLn1F_4:Yb^{3+}/Ln2^{3+} (Ln1 = Y, Lu; Ln2 = Er, Ho, Tm, Eu) disks and analyzed the reasons for the differences in the luminescence intensity of $NaYF_4$ and $NaLuF_4$.[44] Gao et al. studied the UCL properties of single $LiYF_4$ and $LiLuF_4$:Yb^{3+}/Ln^{3+} microcrystals (MCs) and analyzed the reasons for the differences in UC emission intensity and R/G ratio.[45] Wisser et al. utilized Gd^{3+} and Lu^{3+} to codope Y^{3+} of $NaYF_4$:Yb/Er, leading to a 1.6-fold enhancement in UC quantum yield.[46] Avram et al. investigated the power dependence of $NaGdF_4$:Yb/Er under pulsed excitation and analyzed the bidirectional energy transfer between Er^{3+} and Gd^{3+}.[47]

Investigating the disparities in the luminescent properties of host matrices containing different alkali metal ions and lanthanide ions is essential. Elucidating the underlying mechanisms is crucial for identifying materials with outstanding UCL capabilities and for exploring diverse application fields. However, previous studies lacked a comprehensive consideration of the effects of alkali metal ions and lanthanide ions on the crystal field, with a single variable setting. Additionally, most comparative dimensions focused on only steady-state UC emissions under continuous wave (CW) excitation, concentrating on specific emission bands (red and green emission). It is proved that $NaYF_4$:Yb/Er exhibits "multiband" UC emissions under high-power excitation.[48] Pulsed lasers can achieve a higher peak power compared to that of CW and reduce the luminescence quenching caused by local thermal effects. However, in the discussion of the UCL dynamics excited by a pulsed laser, the focus is often only on the attenuation of luminescence.

In this work, we used a 976 nm high-power ns-pulsed laser to excite Yb−Er codoped $NaLnF_4$ and $LiLnF_4$ (Ln: Y, Lu, and Gd) MCs and discussed the multiband UC dynamics in detail. The effects and mechanisms of different alkali metal ions and lanthanide host lattice ions on the rise and decay of UC emission, electron population pathway, energy transfer process, and wavelength intensity distribution in Yb−Er luminescent systems were analyzed. Our research is anticipated to serve as a reference for identifying superior alternatives to $NaYF_4$ in rapid-response optoelectronic devices, micro−nano lasers, and stimulated emission depletion (STED) microscopy.

2. EXPERIMENTAL SECTION

2.1. Sample Preparation. $AREF_4$ MCs were synthesized by using the hydrothermal method. The doping habits of lanthanide ions in various host lattices are different. In general, the closer the radius of the dopant ion is to the lattice ion radius, the easier it is to dope. The ionic radii of Yb^{3+}, Er^{3+}, Y^{3+}, Lu^{3+}, and Gd^{3+} are 85.8, 88.1, 90, 84.8, and 93.8 pm, respectively. For $NaLuF_4$, due to the smaller radius of Lu^{3+} compared to those of Yb^{3+} and Er^{3+}, lattice expansion occurs when Yb^{3+} and Er^{3+} replace the lattice position of Lu^{3+}. Therefore, under the same preparation conditions, $NaLuF_4$ tends to have dimensions larger than those of $NaYF_4$. On the other hand, $NaGdF_4$ is the opposite, with Gd^{3+} having a larger radius than Yb^{3+} and Er^{3+}. The doping of Yb^{3+} and Er^{3+} can cause lattice shrinkage, resulting in $NaGdF_4$ having a smaller size than $NaYF_4$ under the same preparation conditions. Therefore, to achieve uniform size, we endeavored to synthesize diverse inorganic matrices using varying conditions, including quantities of raw materials, temperatures, and reaction durations. The preparation procedures for each sample are delineated as follows:

2.1.1. $NaYF_4$:20%Yb,2%Er. A total of 1 mmol of rare earth chloride (0.78 mmol of $YCl_3{\cdot}6H_2O$, 0.02 mmol of $ErCl_3{\cdot}6H_2O$, and 0.2 mmol of $YbCl_3{\cdot}6H_2O$) was dissolved in 22 mL of deionized water and stirred for 30 min. Subsequently, 1 mmol of EDTA-Na was added and stirred for another 30 min, followed by the addition of 6 mmol of solid NaF (as the fluoride source) and continued stirring for 30 min. The resulting mixture was then transferred to a 30 mL stainless steel autoclave and reacted at 180 °C for 24 h.

2.1.2. $NaLuF_4$:20%Yb,2%Er. A total of 1 mmol of rare earth chlorides, comprising 0.78 mmol of $LuCl_3{\cdot}6H_2O$, 0.02 mmol of $ErCl_3{\cdot}6H_2O$, and 0.2 mmol of $YbCl_3{\cdot}6H_2O$, was dissolved in 22 mL of deionized water and stirred for 30 min. Subsequently, 1 mmol of EDTA-Na was added and stirred for another 30 min. This was followed by the addition of 6 mmol of NaF and continued stirring for 30 min. The resulting mixture was then transferred to a 30 mL stainless steel autoclave and reacted at 130 °C for 24 h. Previous research has shown that higher temperatures are conducive to the synthesis of larger particles.[49,50] Consequently, we decreased the reaction temperature from 180 °C for $NaYF_4$ to 130 °C.

2.1.3. $NaGdF_4$:20%Yb,2%Er. A total of 1 mmol of rare earth chloride, comprising 0.78 mmol of $GdCl_3{\cdot}6H_2O$, 0.02 mmol of $ErCl_3{\cdot}6H_2O$, and 0.2 mmol of $YbCl_3{\cdot}6H_2O$, was dissolved in 22 mL of water and stirred for 30 min. Subsequently, 1 mmol of EDTA was added and stirred for another 30 min. This was followed by the addition of 8 mmol of NaF and continued stirring for 30 min. The resulting mixture was transferred to a 30 mL stainless steel autoclave and reacted at 180 °C for 24 h. To enlarge the size of $NaGdF_4$, we endeavored to increase the amount of NaF and substitute EDTA-Na with EDTA.

2.1.4. $LiYF_4$:20%Yb,2%Er. A total of 1 mmol of rare earth chloride, consisting of 0.78 mmol of $YCl_3{\cdot}6H_2O$, 0.02 mmol of $ErCl_3{\cdot}6H_2O$, and 0.2 mmol of $YbCl_3{\cdot}6H_2O$, was dissolved in 22 mL of water and stirred for 30 min. Subsequently, 1 mmol of EDTA-Na was added and stirred for another 30 min. This was followed by the addition of 3 mmol of NaF and 3 mmol of LiF (it was proved that the addition of Na ions enhances the crystallinity of $LiYF_4$), with continued stirring for 30 min. The resulting mixture was transferred to a 30 mL stainless steel autoclave and reacted at 180 °C for 24 h.

2.1.5. $LiLuF_4$:20%Yb,2%Er. A total of 1 mmol of rare earth chloride (0.78 mmol of $LuCl_3{\cdot}6H_2O$, 0.02 mmol of $ErCl_3{\cdot}6H_2O$, and 0.2 mmol of $YbCl_3{\cdot}6H_2O$) was dissolved in 22 mL of water and stirred for 30 min. Subsequently, 1 mmol of EDTA-Na was added and stirred for another 30 min, followed by the addition of 6 mmol LiF and continued stirring for 30 min. The resulting mixture was then transferred to a 30 mL stainless steel autoclave and reacted at 180 °C for 24 h.

After the reaction, these samples were naturally cooled to room temperature, washed three times with deionized water, and then dispersed in ultrapure water for further use.

2.2. Sample Characterization. The crystal structure and morphology of the samples were analyzed using X-ray diffraction (XRD), scanning electron microscopy (SEM), and inductively coupled plasma optical emission spectrometry

https://doi.org/10.1021/acsomega.4c05453
ACS Omega 2024, 9, 39893−39903

(ICP-OES). SEM images of the samples were obtained using a ZEISS Sigma 300. Figure 1 displays the SEM images and

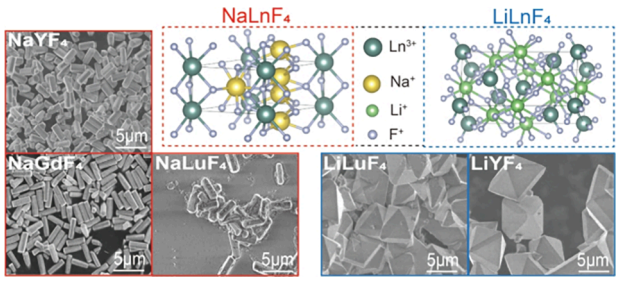

Figure 1. SEM images and crystal structures of the $AREF_4$:Yb/Er MCs.

crystal structures of $NaLnF_4$ and $LiLnF_4$ MCs. Meanwhile, we counted the sizes of approximately 100−150 MCs and calculated their particle size distribution. The results are shown in Figure S2. It is evident that the MCs of $NaYF_4$, $NaLuF_4$, and $NaGdF_4$ exhibit a uniform rod-like structure, with average dimensions of approximately 2−3 μm in length, 0.6−1.3 μm in diameter, and an aspect ratio of about 3−4. Conversely, the MCs of $LiYF_4$ and $LiLuF_4$ possess an octahedral structure comprising eight triangular faces, with an average diagonal length of about 12 μm and each side of the triangle measuring about 6 μm. Previous studies have shown that the luminescence intensity of UC particles at the nanoscale exhibits a size-dependent relationship, but there have been no reports on the size effects at the micrometer scale.[51−56] Obviously, the particle sizes of the same alkali metal ion matrix are similar. However, $LiLnF_4$ has a larger particle size than $NaLnF_4$, making it difficult to consider which of lattice ions and size dominates the UCL intensity. Based on this, the comparison in this article is mainly based on the normalized intensity, the proportion of UCL intensity at each wavelength, and the establishment and attenuation process of multiphoton emission. Powder XRD (40 kV and 40 mA, CuKR, Rigaku Smartlab SE) was used for crystal-phase identification. The scan was performed in the 2θ range 5−90° at a rate of 1°/min. The refinement of XRD data used the Topas Academic software (based on the Rietveld method). Figure 2 shows the refined XRD spectra of $AREF_4$ MCs. Using the Rietveld method, we analyzed the structures (Figure S3), cell constant, and bond lengths (Tables S1 and S2) of the different crystals in detail. The crystals of the three Na-based $AREF_4$ exhibit pure hexagonal phase structures, while the crystals of the two Li-based $AREF_4$ display tetragonal phase structures with high crystallinity. ICP-OES was conducted using an Agilent 5110 at a pump rate of 60 r/min. The results are shown in Table S3. The ratio of Yb and Er is close to 10, but due to the different doping habits of lanthanide ions in various host lattices, this value varies slightly in different matrices.

Steady-state photoluminescence was measured using an Edinburgh FLS1000 spectrometer excited by a 976 nm continuous laser. Absolute UC quantum yield is calculated in Figure S1. Transient photoluminescence measurements were conducted using an intensified charge-coupled device (ICCD)-equipped spectrometer by precisely controlling the gate width and time delay via a digital delay generator (DDG). The excitation source is a 976 nm nanosecond-pulsed laser with a 15 ns pulse width, operated at a repetition frequency of 45 Hz. The excitation power density is approximately 0.16 GW/cm^2.

3. RESULTS AND DISCUSSION

3.1. Impact of Alkali Metal Ions. Initially, we measured the UCL spectrum of $AREF_4$ within 1 ns after the laser pulse,

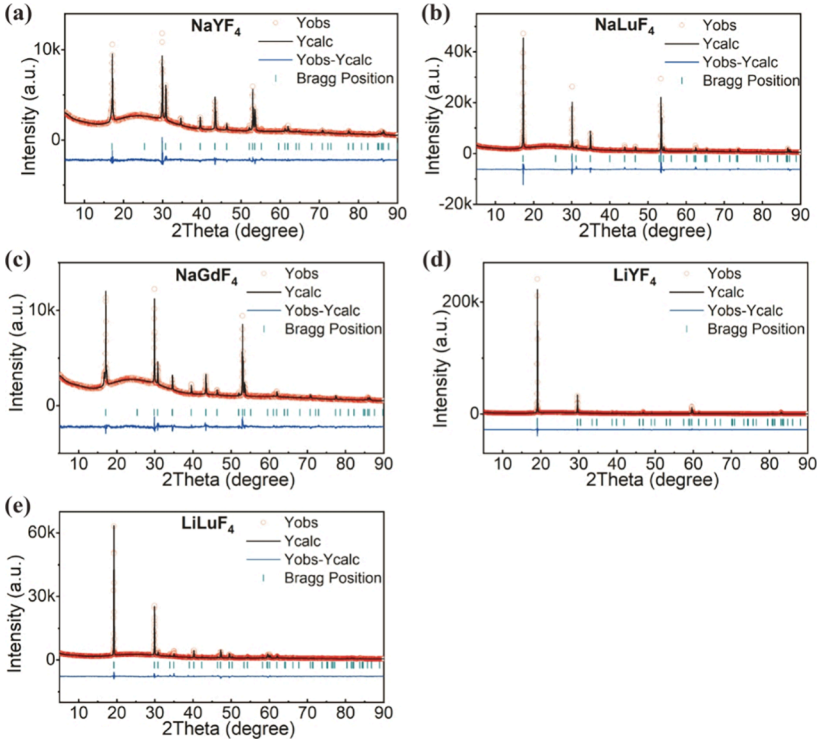

Figure 2. (a−e) Refined X-ray diffraction (XRD) spectra of $AREF_4$ microcrystals (Rietveld method).

https://doi.org/10.1021/acsomega.4c05453
ACS Omega 2024, 9, 39893−39903

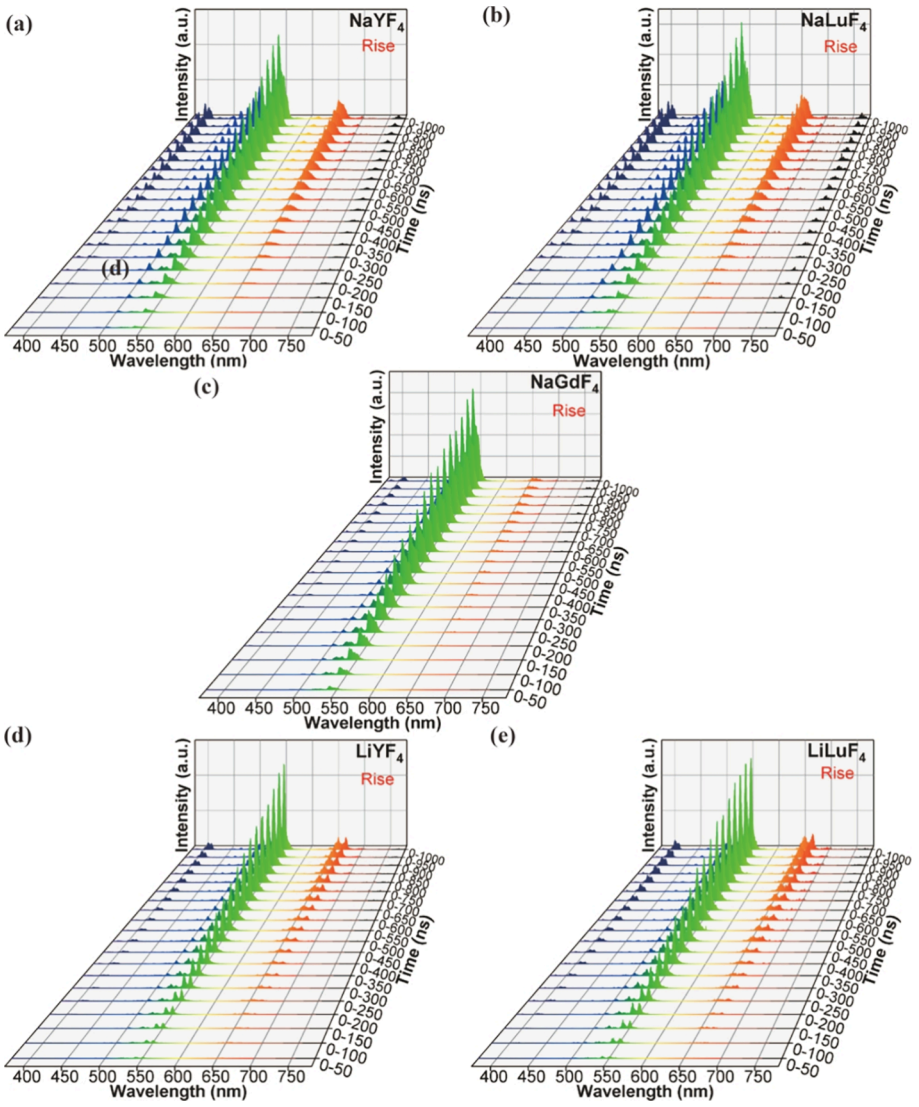

Figure 3. (a–e) Transient UCL spectra of $AREF_4$:Yb/Er MCs within 1 μs after excitation.

with a step size of 50 ns. As depicted in Figure 3a–e, the luminescence dynamics and spectral morphologies vary among different host matrices. The energy level transitions corresponding to different emission wavelengths are labeled in Figure 4a. Under consistent conditions of lanthanide-doped ions (Y^{3+}, Lu^{3+}), the Na-based host matrix exhibits a higher relative intensity at 384 nm ($^4G_{11/2} \rightarrow {}^4I_{15/2}$), 402 nm ($(^2P,^2D,^4F)_{3/2} \rightarrow {}^4I_{13/2}$), 470 nm ($(^2P,^2D,^4F)_{3/2} \rightarrow {}^4I_{11/2}$), and 767 nm ($(^2P,^2D,^4F)_{3/2} \rightarrow {}^4S_{3/2}$) compared to the Li-based host matrix, with faster luminescence buildup. Over a longer time range (5 and 20 μs in Figure 4b,c), the spectral morphology of the same alkali metal host matrix with different lanthanide-doped ions is similar, indicating that Lu^{3+} and Y^{3+} are optically inert and do not participate in energy absorption and transfer. The spectral morphology of different alkali metal host matrices differs significantly, with the Na-based host matrix showing more significant multiband UC emission and the Li-based host matrix exhibiting obvious spectral splitting. The studied Na-based host matrix phase is hexagonal, while the Li-based host matrix phase is tetragonal, and their phonon energies differ. Under the weak coupling approximation of photon–phonon, lower phonon energy corresponds to a lower multiphonon relaxation rate.[57−59] $NaYF_4$ and $NaLuF_4$ have lower phonon energies, resulting in a lower nonradiative transition rate, effectively increasing the radiation transition probability of different energy levels. This hinders inefficient energy dissipation and avoids concentrating energy on the primary emissions of red and green, thereby achieving multicolor UCL within the visible light spectrum.

Then, we investigated the sequence of the UC pathway of Er^{3+} energy levels on Na-based and Li-based host matrices, as depicted in Figure 4d. Previous studies have demonstrated the multiband emission of Yb–Er codoped systems under strong light excitation. They classified each wavelength based on the number of photons absorbed for UC emission and explored the energy transfer and UC pathways between Yb^{3+} and Er^{3+}.[48,60,61] Here, we categorized the UC pathways into two, labeled as A and B, based on the number of photons absorbed during the UC process and the presence of a nonradiative process. The 976 nm laser energy is absorbed by sensitizer Yb^{3+} and transferred to Er^{3+} through the energy transfer upconversion (ETU) process. $^2G_{7/2}$ was populated via pathways A-1, A-2, and A-3 in sequence. Then, in the Na-based host matrix, pathway A-4 takes precedence over B-2, whereas the opposite is observed in the Li-based host matrix. This result can be explained from two aspects. First, the

https://doi.org/10.1021/acsomega.4c05453
ACS Omega 2024, 9, 39893−39903

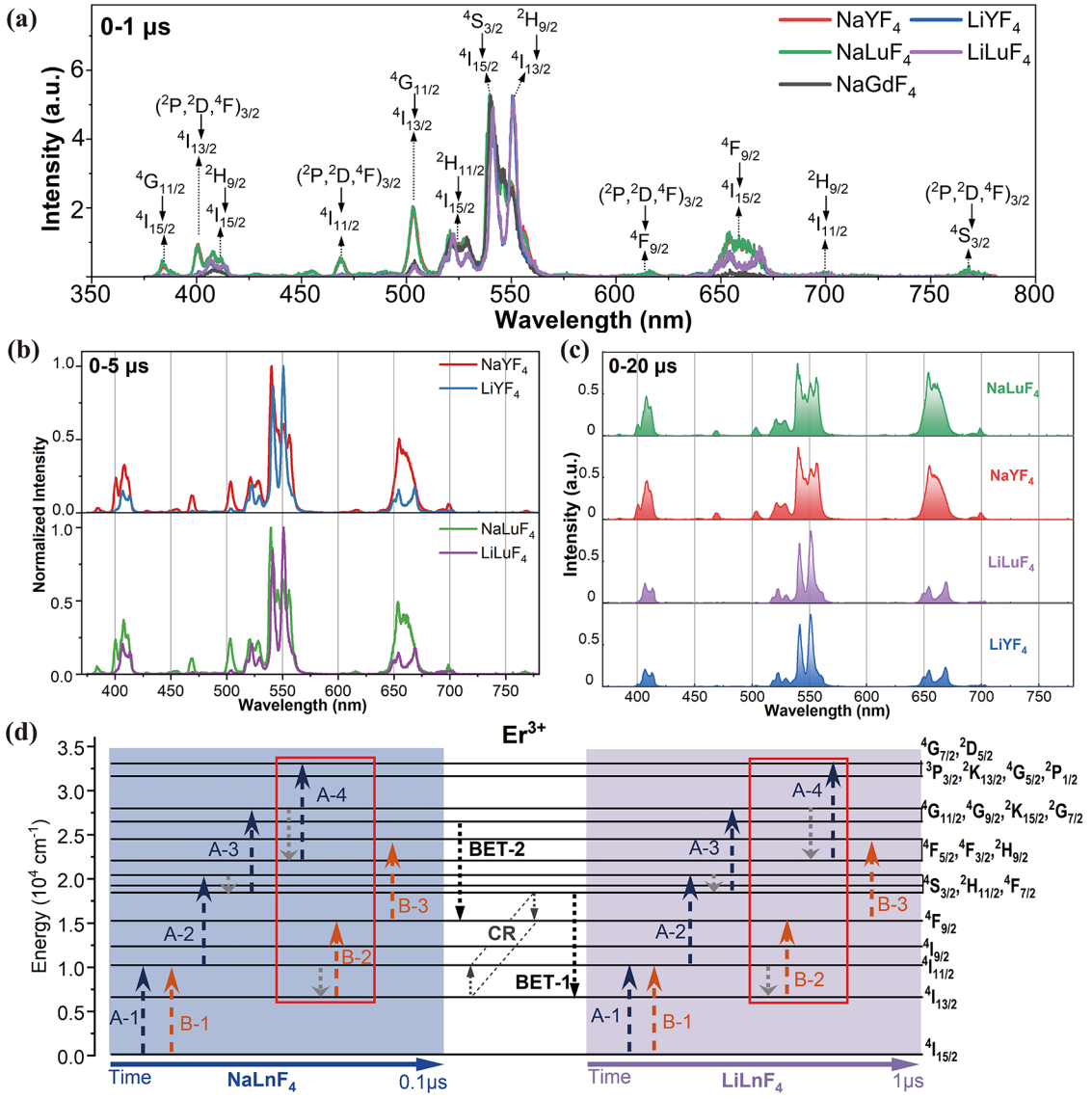

Figure 4. (a) UCL spectra of $AREF_4$:Yb/Er (A = Na/Li, RE = Y/Lu/Gd) microcrystals (MCs) in 0−1 μs (the transition energy levels corresponding to different emission peaks are marked above); UCL spectra of $AREF_4$:Yb/Er (A = Na/Li, RE = Y/Lu) MCs in 0−5 μs (b) and 0−20 μs (c); (d) sequence of UC pathways in $NaLnF_4$ and $LiLnF_4$ MCs (A/B: UC pathways; the number after the letter represents the amount of photons that need to be absorbed during the UC process; BET, back energy transfer; CR, cross relaxation).

different crystal phases result in different phonon energies for the two host matrices. The Na-based host matrix has lower phonon energy, leading to a lower nonradiative transition rate. On one hand, intermediate energy levels are more likely to absorb photons and achieve a population of high energy levels, while in the Li-based host matrix, the depopulation of intermediate energy levels leads to a lower UC efficiency. On the other hand, for the energy gap of 3609 cm^{-1} between $^4I_{11/2}$ and $^4I_{13/2}$, the number of phonons required for multiphonon relaxation is smaller under the Li-based host matrix, leading to a higher probability of relaxation from $^4I_{11/2}$ to $^4I_{13/2}$, thus giving a higher priority to pathway B-2.

As depicted in Figure 5a, we categorized the UCL characteristic wavelengths of $AREF_4$:Yb/Er MCs into three groups (two-photon, three-photon, and four-photon UC emission) based on the number of absorbed photons and analyzed the ETU, back ET (BET), and bidirectional ET (Bid-ET) processes in the Yb−Er system. We evaluated the UCL proportion of the three-photon and four-photon processes within 10 μs after laser pulse excitation (as shown in Figure 5b,c). When calculating the three-photon group, we excluded the UC emission at 558 nm ($^2H_{9/2}\rightarrow {}^4I_{13/2}$) because of potential spectrum broadening from different MCs, which may be associated with the UC emission at 542 nm ($^4S_{3/2}\rightarrow {}^4I_{15/2}$). This treatment has no impact on the overall UC emission variation of the three-photon group. Evidently, within 10 μs, under consistent conditions of lanthanide-doped ions (Y^{3+}, Lu^{3+}), the percentage intensity of three-photon and four-photon emissions in the Na-based host matrix surpasses that in the Li-based host matrix, reaching its peak within 1 μs and subsequently declining. Conversely, the percentage intensity of three-photon and four-photon emissions in the Li-based host matrix fluctuates and increases within 10 μs. This observation supports the earlier explanation: the relatively high UC efficiency of the Na-based host matrix promotes the occurrence of three-photon and four-photon UC processes,

https://doi.org/10.1021/acsomega.4c05453
ACS Omega 2024, 9, 39893−39903

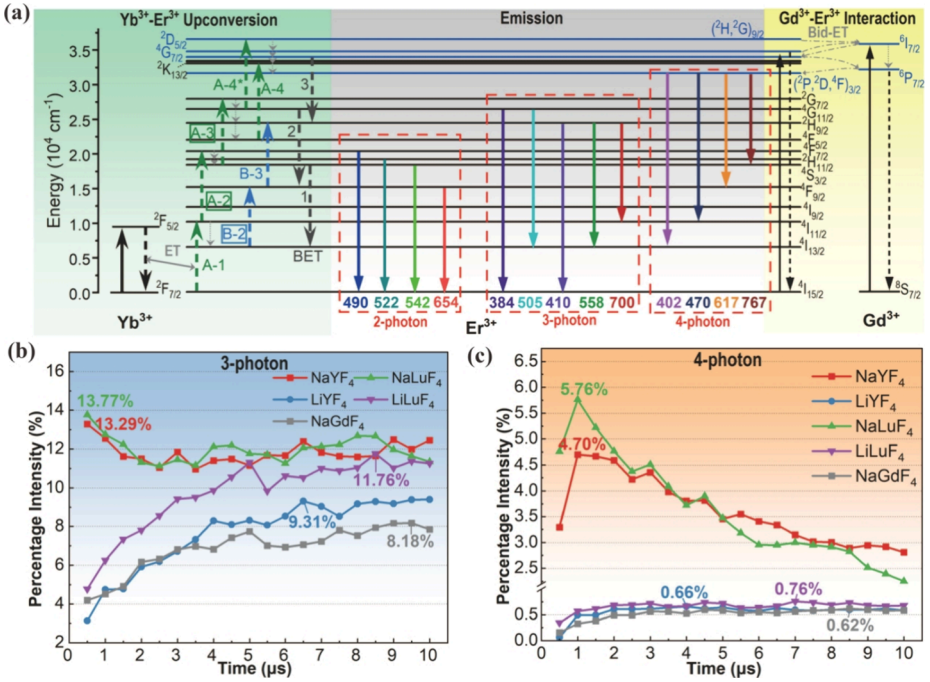

Figure 5. (a) Energy level structure and ET pathways in Yb−Er codoped systems (colorful dashed arrows, gray dashed arrows, and colorful solid arrows represent UC pathways, nonradiative transitions, and UC emissions, respectively; the mutiphoton UC emission is marked with red dashed boxes); percentage intensity of three-photon (b) and four-photon (c) UC emissions in 0−10 μs.

leading to more population at higher energy levels within a short time. Simultaneously, the lower nonradiative process rate enhances the probabilities of radiative transition from high energy levels to the ground state. It is noteworthy that over time, the percentage intensity of the three-photon emission in the Li-based host matrix tends to approach that of the Na-based host matrix, while the percentage intensity of the four-photon emission remains notably distinct from that of the Na-based host matrix. By separately analyzing the contributions of the A-3 pathway ($^4S_{3/2}\rightarrow {}^2G_{7/2}$) and A-4 pathway ($^4F_{5/2}\rightarrow {}^2P_{1/2}$) to the three-photon and four-photon emissions, we can use the percentage intensity of these emissions to characterize the "execution rate" of the A-3 and A-4 pathways. The nonradiative transition from $^4S_{3/2}$ to $^4F_{9/2}$ is unlikely to occur due to the substantial energy gap between these two levels. Consequently, the execution rate of the A-3 pathway is not expected to vary significantly. In contrast, the population of $^4F_{5/2}$, crucial for the A-4 pathway, experiences heightened phonon energy impact due to the narrow energy gap with $^4F_{7/2}$. Therefore, the probability of a nonradiative transition from $^4F_{5/2}$ to $^4F_{7/2}$ in a Li-based matrix is larger than in a Na-based matrix. As a result, the execution rate of the A-4 pathway in a Na-based matrix surpasses that in a Li-based matrix. This explanation is also an important reason for the difference in the spectral morphology between the two host matrices.

3.2. Impact of Doped Ln^{3+} (Y^{3+}, Lu^{3+}, Gd^{3+}). Figure 4a−c shows that the spectra of AYF_4 and $ALuF_4$ (A= Na and Li) do not significantly differ. Due to the mismatch in energy levels, Y^{3+} and Lu^{3+} are not directly involved in the ET within the Yb−Er system. However, according to Figure 5b,c, under the same alkali metal host matrix, the intensity of the three-photon and four-photon emission of $ALuF_4$ is almost greater than that of AYF_4 within 5 μs after pulsed laser excitation. This indicates that Lu^{3+} can effectively increase the energy acquired by Er^{3+}, allowing a greater population of higher energy levels through the A-3 and A-4 pathways. Since the excitation condition and Yb^{3+} concentration are the same, the energy absorption efficiency of Yb^{3+} does not significantly differ. However, ET between Yb^{3+} and Er^{3+} is influenced by the crystal field environment. The ionic radii of Y^{3+} and Lu^{3+} differ, leading to varying distances between the two ions when they are arranged in a lattice. After Yb^{3+} and Er^{3+} replace their original lattice positions, the distances between Yb^{3+} and Er^{3+} are different. The radius of Lu^{3+} is smaller than that of Y^{3+}. As shown in Tables S1 and S2, the minimum distance from Yb^{3+} to Er^{3+} (the same as the minimum distance from Yb^{3+} to Yb^{3+}) of $NaLuF_4$ (3.4552(3) Å) and $LiLuF_4$ (3.68354(12) Å) is smaller than that of $NaYF_4$ (3.50920(16) Å) and $LiYF_4$ (3.71829(0) Å). Therefore, the ET distance in the Yb−Er system of $NaLuF_4$ and $LiLuF_4$ is shorter, which can effectively reduce energy dissipation and increase the efficiency of ET from Yb^{3+} to Er^{3+}. Previous studies have shown that the crystal field symmetry of $ALuF_4$ is weaker than that of AYF_4.[44] According to the J-O theory, it results in a larger Ω_2 parameter and enhanced hypersensitive transitions.[45] Meanwhile, the bond length between Lu^{3+} and F^- (2.3578 Å) is shorter, leading to an overlap of electron clouds, which increases the Ω_4 and Ω_6 parameters, thereby increasing the probability of insensitive radiative transitions, making the UC efficiency of $ALuF_4$ higher.

The UCL properties of $NaGdF_4$ are significantly different from those of $NaYF_4$ and $NaLuF_4$ MCs. From Figure 3a−c, $NaGdF_4$ does not show significant multiband UC emission. Compared to $NaYF_4$ and $NaLuF_4$, the UC emission time of $NaGdF_4$ is later. It can be seen from Figure 5b,c that the intensity of the three-photon and four-photon UC emissions of $NaGdF_4$ is weaker than that of $NaYF_4$ and $NaLuF_4$, indicating a lower execution rate of the A-3 and A-4 (A-4*) pathways. Specifically, the three-photon emission of $NaGdF_4$ gradually increases within 10 μs, indicating the lower ET efficiency

https://doi.org/10.1021/acsomega.4c05453
ACS Omega 2024, 9, 39893−39903

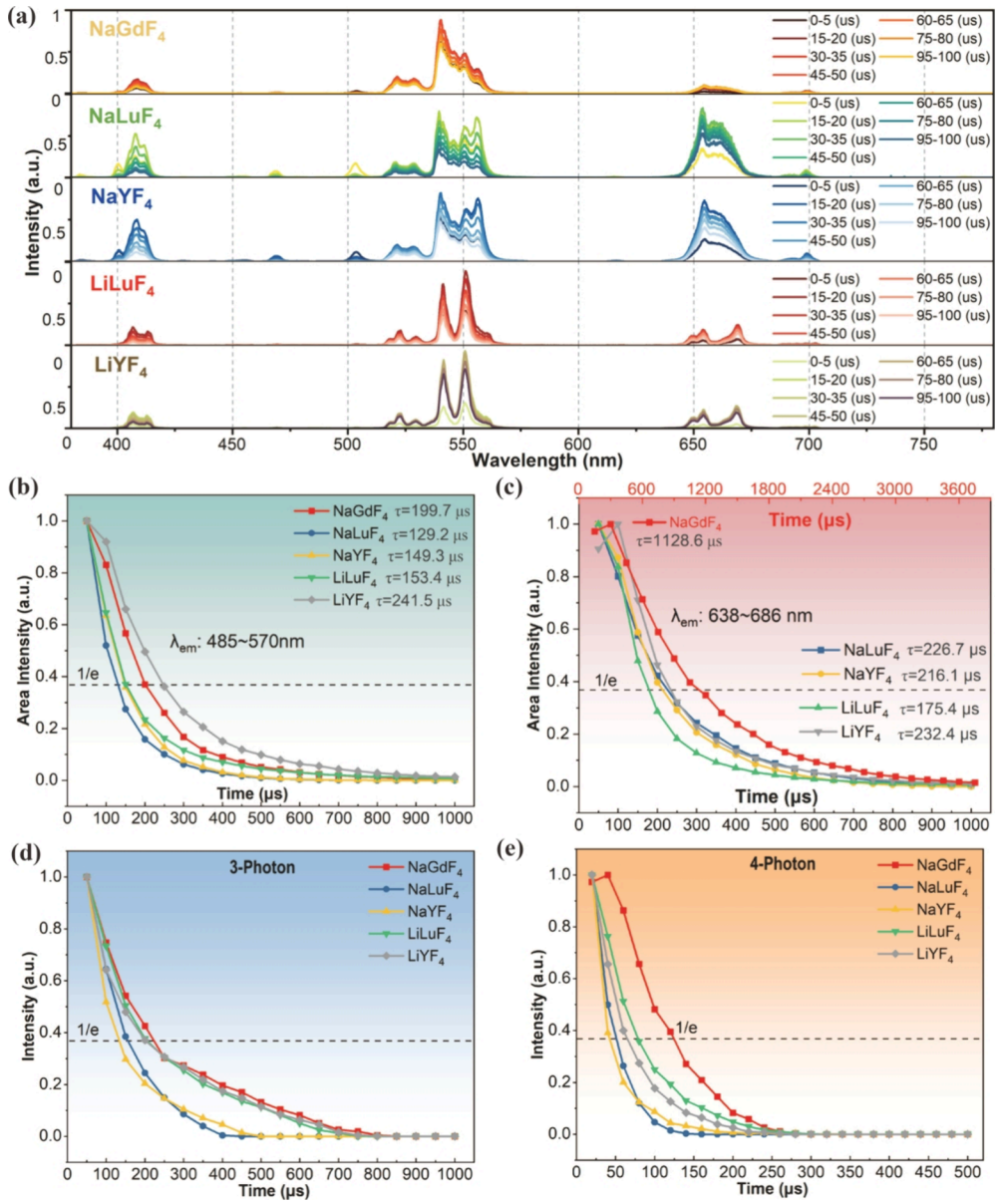

Figure 6. (a) Transient UCL spectra of $AREF_4$:Yb/Er MCs within 100 μs after excitation. Intensity decay curves of different luminescence components in $AREF_4$:Yb/Er MCs: (b) green emission; (c) red emission (the time scale of $NaGdF_4$ is indicated above the figure in red); (d) three-photon emission; (e) four-photon emission.

between Yb^{3+} and Er^{3+}. Combining with the previous analysis, the radius of Gd^{3+} is 93.8 pm, larger than those of Y^{3+} (90 pm) and Lu^{3+} (84.8 pm), resulting in a larger ET distance in the Yb−Er system and lower UC efficiency. The four-photon emission remains at a relatively low level within 10 μs, with a few variations in amplitude. If only from the perspective of ET efficiency, the abrupt decline compared to those of $NaYF_4$ and $NaLuF_4$ cannot be explained. According to Avram et al.'s research,[47] the $^6I_{7/2}$ and $^6P_{7/2}$ of Gd^{3+} will couple with the $^2D_{5/2}$, $^4G_{7/2}$, and $(^2P, ^2D, ^4F)_{3/2}$ of Er^{3+}, causing the transitions of Er^{3+}:$^2D_{5/2}$ + Gd^{3+}:$^8S_{7/2}$→ Er^{3+}:$^4I_{15/2}$ + Gd^{3+}:$^6I_{7/2}$ and Er^{3+}:$^2G_{7/2}$, $(^2P, ^2D, ^4F)_{3/2}$ + Gd^{3+}:$^8S_{7/2}$→ Er^{3+}:$^4I_{15/2}$ + Gd^{3+}:$^6P_{7/2}$. This process reduces the electron population of $(^2P, ^2D, ^4F)_{3/2}$, leading to a significant decrease in four-photon UC emission.

3.3. Luminescence Decay Dynamics. Figure 6a shows the UCL spectra of $AREF_4$ within 100 μs of laser pulse excitation. The UCL intensity of all samples starts to decrease between 20 and 30 μs. Notably, the spectral morphology of $NaGdF_4$ differs significantly from that of $NaYF_4$ and $NaLuF_4$. This is due to the involvement of Gd^{3+} in the ET within the Yb−Er system, which consequently alters the distribution of the UCL intensity across various wavelengths. The onset of UCL decay in AYF_4 and $ALuF_4$ varies, with these variances linked to the luminescent environment created by Y^{3+} and Lu^{3+} acting as lattice ions in the Yb−Er system. Then, we examined the decay characteristics of various luminescent components. This included the decay of cyan and green emissions (Figure 6b) within the wavelength range of 485−570 nm, the decay of red emission (Figure 6c) within the range of 638−686 nm, three-photon UC emission (Figure 6d) excluding 505 nm ($^4G_{11/2}$→$^4I_{13/2}$) and 558 nm, and four-photon UC emission (Figure 6e). Meanwhile, we measured the UCL spectra of $AREF_4$ within an integration time of 0−1 ms (Figure 7a) and

https://doi.org/10.1021/acsomega.4c05453
ACS Omega 2024, 9, 39893−39903

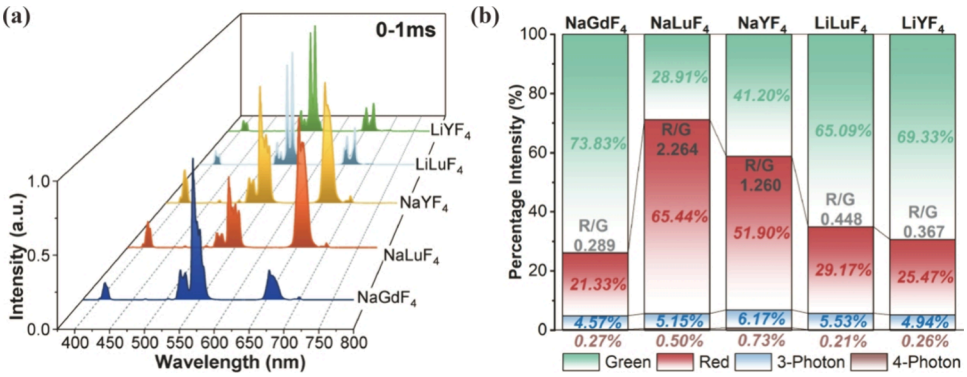

Figure 7. (a) UCL spectra of $AREF_4$:Yb/Er MCs in 0−1 ms; (b) percentage intensity of different luminescence components of $AREF_4$:Yb/Er MCs in 0−1 ms.

calculated the proportions of the different emission components (Figure 7b). It is important to note that in this context, "green" refers to the green emission ranging from 515 to 570 nm, while "red" refers to the red emission within the 638−686 nm range. Additionally, "three-photon" excludes the emission at 558 nm. Significant variations in the UCL components of different host matrices are evident in Figure 7b. $NaGdF_4$ has the highest proportion of green emission, and the lowest is $NaLuF_4$; $NaLuF_4$ has the highest proportion of red emission, and the lowest is $NaGdF_4$. The green emission (542 nm) comes from the two-photon UC process (A-2 pathway), while the red emission comes from the combined effect of the two-photon and three-photon UC processes. As shown in Figure 5a, the UC pathways contributing to the red emission are marked with borders. The BET process (Er^{3+}:$^4G_{11/2}$ + Yb^{3+}:$^2F_{7/2}$ → Er^{3+}:$^4F_{9/2}$ + Yb^{3+}:$^2F_{5/2}$) from Er^{3+} to Yb^{3+} is also affected by the ET distance. The longer ET distance between Yb and Er in $NaGdF_4$ not only weakens the UC efficiency (the proportion of three-photon and four-photon emission is the lowest) but also suppresses the contribution of the three-photon UC process to red emission. The strongest red emission in $NaLuF_4$ is due to its shortest ET distance. The proportion of three-photon and four-photon emission in $NaYF_4$ is higher than in $NaLuF_4$, because the ET distance in its system is slightly larger than that in $NaLuF_4$, alleviating the "weakening effect" of the BET-2 and BET-3 processes on the population of high-energy state electrons. When the lanthanide lattice ions are Y^{3+} and Lu^{3+}, there is a significant difference in the R/G ratio in different alkali metal ion matrices. The R/G ratio of the Li-based host matrix is significantly smaller than that of the Na-based host matrix. This difference may be attributed to the minimal observation of emission at 384 and 505 nm in $LiLnF_4$ experiments. As shown in Figure 5a, the three-photon emission of $LiLnF_4$ mainly originates from 410 nm ($^2H_{9/2}$→ $^4I_{15/2}$) and 700 nm ($^2H_{9/2}$→ $^4I_{11/2}$) (with 558 nm included in the green emission), suggesting that the A-3 pathway is less efficient than the B-3 pathway. Alternatively, this variation may result from the high nonradiative transition rate and the lower electron population in $^4G_{11/2}$, which weakens the BET-2 process and reduces the contribution of the three-photon UC process to red emission. Furthermore, Wang et al. suggested that differences in the −OH group of EDTA in various alkali metal ion matrix environments may lead to variations in R/G.[42] Meanwhile, the four-photon emission proportion in $LiLnF_4$ is lower than that in $NaLnF_4$, further demonstrating the enhancement effect of the Na-based matrix environment on UC efficiency.

From Figure 6b−e, it can be seen that the decay rate of green emission of the same alkali metal ion matrix is related to its intensity ratio. $LiYF_4$ and $NaGdF_4$ have the highest UCL proportion of green emission and exhibit the slowest decay of green emission, which reflects the efficiency of the A-2 pathway in different samples and thereby results in a relatively longer lifetime of the corresponding UC emission. The decay mechanism of red emission differs from that of green. In $NaLnF_4$, the lifetime of red emission in $NaLuF_4$ exceeds that in $NaYF_4$, similar to the case of green emission. $NaLuF_4$, with a higher proportion of red emission, leads to a slower decay of the red emission. However, for $LiLnF_4$, despite $LiLuF_4$ having a higher proportion of red emission, its decay rate is faster. This may be due to the lower phonon energy, causing the red emission of the Li-based matrix to mainly rely on the two-photon UC process. Therefore, the enhancement effect of Lu^{3+} on red emission is relatively weak and its inhibitory effect on the decay is also not significant. Conversely, the shorter Yb−Er ET distance leads to a faster peak and decay of red emission. $NaGdF_4$ exhibits the longest red emission lifetime, nearly five times longer than that of $NaYF_4$. Additionally, its three-photon and four-photon emission lifetimes surpass those of other samples. Considering the energy level coupling between Er^{3+} and Gd^{3+}, after accumulating a certain number of electrons in the $^6I_{7/2}$ and $^6P_{7/2}$ levels of Gd^{3+}, the transition from $^6I_{7/2}$ and $^6P_{7/2}$ to $^8S_{7/2}$ occurs, filling the $(^2P, ^2D, ^4F)_{3/2}$ of Er^{3+} through resonance ET, and lower energy levels of Er^{3+} through nonresonance ET. This process continuously replenishes the electron population for three-photon and four-photon UC emissions, achieving the "ultra-long lifetime" of red emission via the BET process. Additionally, when the main lattice ions of lanthanides are Lu^{3+} and Y^{3+}, the three-photon and four-photon emission lifetimes in the Na-based matrix are shorter than those in the Li-based matrix. As previously mentioned, the UC efficiency of the Na-based matrix is higher, resulting in a faster completion of the high-energy electron population and consequently shorter durations for three-photon and four-photon UC emission.

4. CONCLUSIONS

In general, under the excitation of a 976 nm high-power ns-pulsed laser, we measured the transient UCL spectrum of $AREF_4$ MCs on the ns scale. The time period after the laser pulse is divided into luminescence rise, development, and decay. From the perspectives of spectral morphology, luminescence emission time, electronic population pathways,

https://doi.org/10.1021/acsomega.4c05453
ACS Omega 2024, 9, 39893−39903

luminescence emission proportion, and luminescence lifetime, the multiband UCL dynamics of Yb−Er codoped systems in different crystal field environments were analyzed. Based on the experimental results, when the lanthanide main lattice ions are optically inert, such as Y^{3+} and Lu^{3+}, the UC efficiency of Na-based matrix MCs is higher due to the low phonon energy and weak crystal field symmetry. This leads to more significant multiband emissions and shorter response times for three-photon and four-photon UC processes, resulting in faster decay. Li-based matrix MCs exhibit a lower R/G ratio and a longer lifetime of green emission ($LiYF_4$). Furthermore, the presence of various lanthanide main lattice ions has a significant impact on the transient UC emission dynamics, attributed to differences in ionic radius and optical sensitivity. The ET distance of Yb−Er systems is $D_{Lu} < D_Y < D_{Gd}$, due to the fact that the ionic radius is $R_{Lu} < R_Y < R_{Gd}$. This results in higher efficiency for three-photon and four-photon UC processes in MCs with Lu^{3+}, but the shorter ET distance exacerbates the BET process of $Er^{3+} \rightarrow Yb^{3+}$, improves the R/G ratio of $ALuF_4$ MCs, and extends the lifetime of red emission ($NaLuF_4$). It is important to note that involvement of the main lattice ions in ET significantly alters the UCL properties. The coupling between Gd^{3+} and Er^{3+} enables bidirectional ET, thereby reducing the contribution of the three-photon UC process to red emission and lowering the R/G ratio. The long lifetimes of $^6I_{7/2}$ and $^6P_{7/2}$ (Gd^{3+}) serve as energy storage reservoirs, prolonging the luminescence duration across different characteristic wavelengths. Specifically, the BET process significantly extends the red emission lifetime of $NaGdF_4$ to approximately five times that of $NaYF_4$. The conclusion shows that $NaLuF_4$ has better performance than $NaYF_4$ in terms of multiband UC response speed, R/G ratio, and red emission lifetime and is expected to be an excellent alternative material to $NaYF_4$ in fast optoelectronic response devices, bioimaging, and multicolor display applications. In comparison to the Na-based matrix, $LiYF_4$ exhibits a lower R/G ratio, more concentrated emission bands, and a longer lifetime of green emission, rendering it suitable as a single-color UC chromogenic agent for green light. Additionally, $NaGdF_4$ exhibits an exceptionally long red luminescence duration, making it a promising candidate for a novel, long-persistent UCL material. Our comparison broadens the utilization of these common inorganic UC materials across various fields and offers a widely applicable method for regulating luminescence. This is anticipated to serve as a reference for identifying superior alternatives to $NaYF_4$ in rapid-response optoelectronic devices, micro−nano lasers, and STED microscopy.

■ ASSOCIATED CONTENT

Supporting Information

The Supporting Information is available free of charge at https://pubs.acs.org/doi/10.1021/acsomega.4c05453.

Detailed sample characterization data; steady-state photoluminescence spectra and absolute UC quantum yield of $AREF_4$ microcrystals (Figure S1); particle size distribution of $AREF_4$ microcrystals (Figure S2); crystal structure and refined XRD data (bond length, bond angle, space group, etc.) of $AREF_4$ microcrystals (Figure S3 and Tables S1 and S2); ICP-OES data of $AREF_4$ microcrystals, showing the rare earth element (Yb, Er) content in the microcrystals (Table S3) (PDF)

■ AUTHOR INFORMATION

Corresponding Authors

Chuan Guo − *College of Advanced Interdisciplinary Studies and Nanhu Laser Laboratory, National University of Defense Technology, Changsha, Hunan 410073, China*; Email: guochuan20@nudt.edu.cn

Kai Han − *College of Advanced Interdisciplinary Studies and Hunan Provincial Key Laboratory of High Energy Laser Technology, National University of Defense Technology, Changsha, Hunan 410073, China*; orcid.org/0000-0001-7689-5339; Email: hankai0071@nudt.edu.cn

Authors

Mingchen Li − *College of Advanced Interdisciplinary Studies and Hunan Provincial Key Laboratory of High Energy Laser Technology, National University of Defense Technology, Changsha, Hunan 410073, China*

Maohui Yuan − *College of Advanced Interdisciplinary Studies, National University of Defense Technology, Changsha, Hunan 410073, China*; orcid.org/0000-0002-4952-4417

Wenda Cui − *College of Advanced Interdisciplinary Studies, National University of Defense Technology, Changsha, Hunan 410073, China*

Hanchang Huang − *College of Advanced Interdisciplinary Studies and Hunan Provincial Key Laboratory of High Energy Laser Technology, National University of Defense Technology, Changsha, Hunan 410073, China*

Complete contact information is available at: https://pubs.acs.org/10.1021/acsomega.4c05453

Notes

The authors declare no competing financial interest.

■ ACKNOWLEDGMENTS

The authors acknowledge the financial support received from the Hunan Provincial Innovation Foundation for Postgraduate (CX20230028).

■ REFERENCES

(1) Pedersen, R. L.; Tidemand-Lichtenberg, P.; Pedersen, a. C. Synchronous Upconversion of Quantum Cascade Lasers in $AgGaS_2$. *Opt. Lett.* **2022**, *47* (21), 5622−5625.

(2) Dupont, H.; Loiko, P.; Tyazhev, A.; et al. Tm:Calgo Lasers at 2.32 μm: Cascade Lasing and Upconversion Pumping. *Opt. Express* **2023**, *31* (12), 18751−18764.

(3) Li, Y.; Liu, K.; Feng, J.; Chen, Y.; Huang, Y.; Zhang, K. Precise Determination of Energy Transfer Upconversion Coefficient for the Erbium and Ytterbium Codoped Laser Crystals. *Opt. Express* **2023**, *31* (26), 44672−44679.

(4) Ji, S.; Lin, X.; Chen, M.; Rong, X.; Xu, H.; Li, W.; Cai, Z. Green Wavelength-Tunable and High Power Ho^{3+}-Doped Upconversion Fiber Lasers. *IEEE Photonics Technol. Lett.* **2020**, *32* (6), 313−316.

(5) Kang, W.; Li, B.; Liang, Y.; Hao, Q.; Yan, M.; Huang, K.; Zeng, H. Coincidence-Pumping Upconversion Detector Based on Passively Synchronized Fiber Laser System. *IEEE Photon. Technol. Lett.* **2020**, *32* (4), 184−187.

(6) Bai, P.; Yang, N.; Chu, W.; et al. Ultra-Broadband Thz/Ir Upconversion and Photovoltaic Response in Semiconductor Ratchet-Based Upconverter. *Appl. Phys. Lett.* **2021**, *119* (24), 1−6.

(7) Yao, H.; Peng, G.; Li, Z.; et al. Unveiling the Origin of Performance Enhancement of Photovoltaic Devices by Upconversion Nanoparticles. *J. Energy Chem.* **2022**, *65* (2), 524−531.

(8) Wang, Q.; Wee, A. T. S. Upconversion Photovoltaic Effect of WS_2/2D Perovskite Heterostructures by Two-Photon Absorption. *ACS Nano* **2021**, *15* (6), 10437−10443.

(9) Ramachari, D.; Esparza, D.; López-Luke, T.; Romero, V. H.; Perez-Mayen, L.; De la Rosa, E.; Jayasankar, C. K. Synthesis of Co-Doped Yb^{3+}-Er^{3+}:ZrO_2 Upconversion Nanoparticles and Their Applications in Enhanced Photovoltaic Properties of Quantum Dot Sensitized Solar Cells. *J. Alloys Compd.* **2017**, *698* (0), 433−441.
(10) Sano, N.; Nishigaya, K.; Tanabe, K. Upconversion Semiconductor Interfaces by Wafer Bonding for Photovoltaic Applications. *Appl. Phys. Lett.* **2022**, *121* (1), No. 011601.
(11) Tadge, P.; Yadav, R. S.; Vishwakarma, P. K.; Rai, S. B.; Chen, T.; Sapra, S.; Ray, S. Enhanced Photovoltaic Performance of Y_2O_3:Ho^{3+}/Yb^{3+} Upconversion Nanophosphor Based Dssc and Investigation of Color Tunability in Ho^{3+}/Tm^{3+}/Yb^{3+} Tridoped Y_2O_3. *J. Alloys Compd.* **2020**, *821* (0), No. 153230.
(12) Tripathi, N.; Ando, M.; Akai, T.; Kamada, K. Efficient Nir-to-Visible Upconversion of Surface-Modified Pbs Quantum Dots for Photovoltaic Devices. *ACS Appl. Nano Mater.* **2021**, *4* (9), 9680−9688.
(13) Wu, H.; Hao, Z.; Zhang, L.; et al. Enhancing Ir to Nir Upconversion Emission in Er^{3+}-Sensitized Phosphors by Adding Yb^{3+} as a Highly Efficient Nir-Emitting Center for Photovoltaic Applications. *CrystEngComm* **2020**, *22* (2), 229−236.
(14) Zeng, J.; Zhang, T.; Liang, G.; et al. A ″Turn Off-On″ Fluorescent Sensor for Detection of Cr(VI) Based on Upconversion Nanoparticles and Nanoporphyrin. *Spectrochim. Acta, Part A* **2024**, *311*, No. 124002.
(15) Lin, G.; Jin, D. Responsive Sensors of Upconversion Nanoparticles. *ACS Sens.* **2021**, *6* (12), 4272−4282.
(16) Mo, J.; Wang, S.; Zeng, J.; Ding, X. Aptamer-Based Upconversion Fluorescence Sensor for Doxorubicin Detection. *J. Fluoresc.* **2023**, *33* (5), 1897−1905.
(17) Zhang, Y.; Guo, Y.; Zheng, X.; Wang, P.; Liu, H. Bright Upconversion Luminescence Performance of Yb^{3+}/Tm^{3+}/Gd^{3+}/Er^{3+} Doped AWO_4 (A = Sr or Ca) Phosphor for Optical Temperature Sensor. *Physica B* **2023**, *649*, No. 414467.
(18) Zhang, X.; Shu, W.; Cheng, M.; Wang, L.; Ran, X. Self-Assembled Ratiometric Sensor for Specific Detection of Hypoxia in Living Cells Based on Lanthanide-Doped Upconversion Nanoparticles and Gold Nanoparticles. *Nanotechnology* **2023**, *34* (41), 415502.
(19) Wang, Z.; Sun, G.; Chen, J.; Xie, Y.; Jiang, H.; Sun, L. Upconversion Luminescent Humidity Sensors Based on Lanthanide-Doped MOFs. *Chemosensors* **2022**, *10* (66), 66.
(20) Ding, C.; Gu, Y.; Chen, W.; Chen, L.; Guo, L.; Huang, Y. Ratiometric Near-Infrared Upconversion Fluorescence Sensor for Selectively Detecting and Imaging of Al^{3+}. *Anal. Chim. Acta* **2023**, *1263*, No. 341297.
(21) Mendonsa, A. A.; Soeldner, C. C.; Mudd, N. E.; Saccomano, S. C.; Cash, K. J. Triplet-Triplet Annihilation Upconversion-Based Oxygen Sensors to Overcome the Limitation of Autofluorescence. *ACS Sens.* **2023**, *8* (8), 3043−3050.
(22) Li, Y.; Li, Y. Highly Sensitive and Quantitative Fluorescent Lateral Flow Strip Sensor for Heart Failure Detecting Based on Dual-Color Upconversion Microparticles. *Ceram. Int.* **2024**, *50* (9), 14318−14325.
(23) Anchante, A.; Puga, R.; Loro, H. $NaYF_4$:Ho^{3+},Yb^{3+}@PEI Upconversion Luminescence Microparticles as Multichannel Optical Sensors for the Identification of Coffee Varieties. *Braz. J. Phys.* **2023**, *53* (5), 115.
(24) Chen, G.; Li, Y.; Liu, J.; Huang, G.; Tian, Q. Anti-Stokes Luminescent Organic Nanoparticles for Frequency Upconversion Biomedical Imaging. *NANOMED-NANOTECHNOL.* **2023**, *50*, No. 102668.
(25) Kang, C.; Zuo, X.; Zhao, L.; et al. Red Emission Upconversion of $NaYF_4$:Yb^{3+}/Er^{3+} Nanoparticles: Rapid Preparation Via Single-Mode Focused Microwave Method and Their Application in Cell Imaging. *Opt. Mater.* **2023**, *143*, No. 114165.
(26) Lu, L.; Song, B.; Gao, J.; Shao, X. A Ratiometric Aptasensor for Simultaneous Determination of Two Estrogens Based on Multicolor Upconversion Nanoparticles. *Sens. Actuators, B* **2023**, *389*, No. 133842.
(27) Lu, Q.; Xie, L.; Yin, S.; et al. Ultrasensitive Detection of Microrna-10b through Target-Triggered Catalytic Hairpin Assembly and Upconversion Nanoparticles-Based Luminescence Resonance Energy Transfer. *Talanta* **2023**, *253*, No. 124032.
(28) Wang, Z.; Liao, C.; Lu, Q.; et al. Glucose-Lightened Upconversion Nanoprobes for Accurate Cellular-Discrimination Based on Warburg Effect. *Anal. Chim. Acta* **2024**, *1296*, No. 342334.
(29) Zhang, N.; Zhang, W.; Wu, Y.; Xie, X.; Jiang, R.; Luo, F.; Zhang, K. Upconversion Nanoparticles Anchored MnO_2 Nanosheets for Luminescence "Turn On" Detecting Hydrogen Peroxide. *Spectrochim. Acta, Part A* **2023**, *299*, No. 122819.
(30) Liang, X.; Zhao, Y.; Cheng, M.; Zhang, F. Rational Design and Synthesis of Upconversion Luminescence-Based Optomagnetic Multifunctional Nanorattles for Drug Delivery. *Chin. J. Chem. Eng.* **2021**, *38* (10), 286−293.
(31) Kamarudin, J. B. M.; Sun, B.; Foo, A. S. C.; et al. Sirius, Ultra-Scintillating Upconversion Breast Implant for Remote Orthotopic Photodynamic Therapy. *ACS Nano* **2023**, *17* (12), 11593−11606.
(32) Zhang, R.; Lu, Y.; Zhou, Y.; et al. Utilizing Dual-Pathway Energy Transfer in Upconversion Nanoconjugates for Reinforced Photodynamic Therapy. *Nano Res.* **2024**, *17* (4), 2941−2948.
(33) Dibaba, S. T.; Xie, Y.; Xi, W.; Bednarkiewicz, A.; Ren, W.; Sun, L. Nd^{3+}-Sensitized Upconversion Nanoparticle Coated with Antimony Shell for Bioimaging and Photothermal Therapy in Vitro Using Single Laser Irradiation. *J. Rare Earths* **2022**, *40* (6), 862−869.
(34) Wang, W.; Li, Q.; Chen, H.; Xie, X.; Li, B.; Kong, X.; Chang, Y. Topological Control of Lanthanide-Doped Upconversion Nanocrystals for Improved Fret Coupling Efficiency in Second near-Infrared-Triggered Photodynamic Therapy. *ACS Appl. Nano Mater.* **2024**, *7* (1), 1045−1054.
(35) Tan, C.; Li, X.; Li, Z.; et al. Near-Infrared-Responsive Nanoplatforms Integrating Dye-Sensitized Upconversion and Heavy-Atom Effect for Enhanced Photodynamic Therapy Efficacy. *Nano Today* **2024**, *54*, No. 102089.
(36) Shi, Z.; Gao, X.; Cai, X.; et al. Fully Implantable and Retrievable Upconversion Waveguides for Photodynamic Therapy in Deep Tissue. *Adv. Opt. Mater.* **2023**, *11* (19), No. 2300689.
(37) Li, Z.; Lu, S.; Li, X.; Chen, Z.; Chen, X. Lanthanide Upconversion Nanoplatforms for Advanced Bacteria-Targeted Detection and Therapy. *Adv. Opt. Mater.* **2023**, *11* (11), 1.
(38) Gong, Y.; Yuan, W.; Zhang, P.; Zheng, K.; Zhang, Q.; Ding, C. A Tumor Targeted Antifouling Upconversion Nanoplatform for Fluorescence Imaging and Precise Photodynamic Therapy Triggered by Nir Laser. *Anal. Chim. Acta* **2023**, *1274*, No. 341561.
(39) Lv, K.; Yao, L.; Fu, X.; et al. Indocyanine Green-Equipped Upconversion Nanoparticles/CeO_2 Trigger Mutually Reinforced Dual Photodynamic Therapy. *Nano Today* **2023**, *52*, No. 101964.
(40) Song, X.; Li, F.; Tian, F.; et al. Upconversion Nanoparticle-Based Optogenetic Nanosystem for Photodynamic Therapy and Cascade Gene Therapy. *Acta Biomater.* **2023**, *157*, 538−550.
(41) Wei, G.; Jun, D.; Rui-Bo, W.; Zhao-Jin, W.; Hai-Rong, Z. Upconversion Flourescence Characteristics of Er^{3+}/Yb^{3+} Codoped $NaYF_4$ and $LiYF_4$ Microcrystals. *Acta Phys. Sin.* **2016**, *65* (8), No. 084205.
(42) Wang, X.; Zhang, X.; Wang, Y.; et al. Comprehensive Studies of the Li^+ Effect on $NaYF_4$:Yb/Er Nanocrystals: Morphology, Structure, and Upconversion Luminescence. *Dalton Trans.* **2017**, *46* (28), 8968−8974.
(43) Tsang, M. Y.; Fałat, P.; Antoniak, M. A.; et al. Pr^{3+} Doped $NaYF_4$ and $LiYF_4$ Nanocrystals Combining Visible-to-UVC Upconversion and NIR-to-NIR-II Downconversion Luminescence Emissions for Biomedical Applications. *Nanoscale* **2022**, *14* (39), 14770−14778.
(44) He, E.; Zheng, H.; Gao, W.; Tu, Y.; Lu, Y.; Li, G. Investigation of Upconversion and Downconversion Fluorescence Emissions from β-$NaLn1F_4$:Yb^{3+}, $Ln2^{3+}$ (Ln1 = Y, Lu; Ln2 = Er, Ho, Tm, Eu) Hexagonal Disk System. *Mater. Res. Bull.* **2013**, *48* (9), 3505−3512.

https://doi.org/10.1021/acsomega.4c05453
ACS Omega 2024, 9, 39893−39903

(45) Gao, W.; Dong, J.; Wang, Z.; Zhang, Z.; Zheng, H. Multicolor Upconversion Emission of Lanthanide-Doped Single $LiYF_4$ and $LiLuF_4$ Microcrystal. *Mater. Res. Bull.* **2017**, *91*, 77−84.
(46) Wisser, M. D.; Fischer, S.; Maurer, P. C.; et al. Enhancing Quantum Yield Via Local Symmetry Distortion in Lanthanide-Based Upconverting Nanoparticles. *ACS Photonics* **2016**, 3 (8), 1523−1530.
(47) Avram, D.; Patrascu, A. A.; Istrate, M. C.; Tiseanu, C. Gd-Er Interaction Promotes $NaGdF_4$:Yb, Er as a New Candidate for High-Power Density Applications. *J. Mater. Chem. C* **2023**, *11* (30), 10409−10419.
(48) Frenzel, F.; Würth, C.; Dukhno, O.; et al. Multiband Emission from Single β-$NaYF_4$(Yb,Er) Nanoparticles at High Excitation Power Densities and Comparison to Ensemble Studies. *Nano Res.* **2021**, *14* (11), 4107−4115.
(49) Purohit, B.; Jeanneau, E.; Guyot, Y.; et al. Incorporation of Upconverting $LiYF_4$:Yb^{3+}, Tm^{3+} Nanoparticles with High Quantum Yield in TiO_2 Metallogels for Near Infrared-Driven Photocatalytic Dye Degradation. *ACS Appl. Nano Mater.* **2023**, *6* (4), 2310−2326.
(50) Mulder, J. T.; Jenkinson, K.; Toso, S.; et al. Nucleation and Growth of Bipyramidal Yb:$LiYF_4$ Nanocrystals−Growing up in a Hot Environment. *Chem. Mater.* **2023**, *35* (14), 5311−5321.
(51) Wong, P. T.; Chen, D.; Tang, S.; et al. Modular Integration of Upconverting Nanocrystal−Dendrimer Composites for Folate Receptor-Specific Nir Imaging and Light-Triggered Drug Release. *Small* **2015**, *11* (45), 6078−6090.
(52) Wang, F.; Wang, J.; Liu, X. Direct Evidence of a Surface Quenching Effect on Size-Dependent Luminescence of Upconversion Nanoparticles. *Angew. Chem., Int. Ed.* **2010**, *49* (41), 7456−7460.
(53) Tanner, P. A.; Duan, C.-K.Size Dependence in Multicolor Upconversion in Single Yb^{3+}, Er^{3+} Co-Doped $NaYF_4$ Nanocrystals. *Physics* **2010**, .
(54) Shan, J.; Uddi, M.; Wei, R.; Yao, N.; Ju, Y. The Hidden Effects of Particle Shape and Criteria for Evaluating the Upconversion Luminescence of the Lanthanide Doped Nanophosphors. *J. Phys. Chem. C* **2010**, *114* (6), 2452−2461.
(55) Chen, C.; Sun, L.-D.; Li, Z.-X.; Li, L.-L.; Zhang, J.; Zhang, Y.-W.; Yan, C.-H. Ionic Liquid-Based Route to Spherical $NaYF_4$ Nanoclusters with the Assistance of Microwave Radiation and Their Multicolor Upconversion Luminescence. *Langmuir* **2010**, *26* (11), 8797−8803.
(56) Song, H.; Sun, B.; Wang, T.; et al. Three-Photon Upconversion Luminescence Phenomenon for the Green Levels in Er^{3+}/Yb^{3+} Codoped Cubic Nanocrystalline Yttria. *Solid State Commun.* **2004**, *132* (6), 409−413.
(57) Zhang, J.; Hao, Z.; Li, J.; Zhang, X.; Luo, Y.; Pan, G. Observation of Efficient Population of the Red-Emitting State from the Green State by Non-Multiphonon Relaxation in the Er^{3+}-Yb^{3+} System. *Light Sci. Appl.* **2015**, *4* (1), No. e239.
(58) Heitz, R.; Veit, M.; Ledentsov, N. N.; et al. Energy Relaxation by Multiphonon Processes in Inas/Gaas Quantum Dots. *Phys. Rev. B* **1997**, *56* (16), 10435−10445.
(59) Weber, M. J. Multiphonon Relaxation of Rare-Earth Ions in Yttrium Orthoaluminate. *Phys. Rev. B* **1973**, *8* (1), 54−64.
(60) Huang, H.; Yuan, M.; Hu, S.; et al. Nanosecond Kinetics of Multiphoton Upconversion in an Optically Trapped Single Microcrystal. *J. Mater. Chem. C* **2022**, *10* (24), 9208−9215.
(61) Würth, C.; Kaiser, M.; Wilhelm, S.; Grauel, B.; Hirsch, T.; Resch-Genger, U. Excitation Power Dependent Population Pathways and Absolute Quantum Yields of Upconversion Nanoparticles in Different Solvents. *Nanoscale* **2017**, *9* (12), 4283−4294.

https://doi.org/10.1021/acsomega.4c05453
ACS Omega 2024, 9, 39893−39903